



Cite this: *Soft Matter*, 2021,  
17, 6603

# Distribution and propagation of mechanical stress in simulated structurally heterogeneous tissue spheroids

Maxim Cuvelier,<sup>id</sup> \*<sup>ab</sup> Jiří Pešek,<sup>ac</sup> Ioannis Papantoniou,<sup>bde</sup> Herman Ramon<sup>a</sup> and Bart Smeets<sup>a</sup>

The mechanical microenvironment of cells has been associated with phenotypic changes that cells undergo in three-dimensional spheroid culture formats. Radial asymmetry in mechanical stress – with compression in the core and tension at the periphery – has been analyzed by representing tissue spheroids as homogeneous visco-elastic droplets under surface tension. However, the influence of the granular microstructure of tissue spheroids in the distribution of mechanical stress in tissue spheroids has not been accounted for in a generic manner. Here, we quantify the distribution and propagation of mechanical forces in structurally heterogeneous multicellular assemblies. For this, we perform numerical simulations of a deformable cell model, which represents cells as elastic, contractile shells surrounding a liquid incompressible cytoplasm, interacting by means of non-specific adhesion. Using this model, we show how cell-scale properties such as cortical stiffness, active tension and cell–cell adhesive tension influence the distribution of mechanical stress in simulated tissue spheroids. Next, we characterize the transition at the tissue-scale from a homogeneous liquid droplet to a heterogeneous packed granular assembly.

Received 15th November 2020,  
Accepted 24th May 2021

DOI: 10.1039/d0sm02033h

[rsc.li/soft-matter-journal](http://rsc.li/soft-matter-journal)

## Introduction

Spheroids – small self-assembled cell aggregates – are an often used culture format to produce micro-tissues and organoids with applications in disease modeling, drug discovery and tissue engineering. They serve as a model to study the mechanisms that govern the organization of cells into tissue, providing *in vitro* analogues to biological processes that occur during tissue development such as cell condensation, jamming, collective migration and sorting.<sup>1,2</sup> Spheroid culture has been shown to alter cell fate compared to two-dimensional cell culture, due to differences in cell morphology resulting in the development of diverse mechanical microenvironments.<sup>3</sup> As cell-generated contractile forces establish the overall mechanical state of tissue spheroids, the resulting force balance is frequently modeled based on the mechanics of a homogeneous viscous or visco-elastic droplet.<sup>4–6</sup> This allows for a straightforward interpretation of mechanical stress, with a compressed core and a tensed periphery that provides surface tension. However, at the

cellular scale, tissue structure is heterogeneous and may feature pores of varying size in a foam-like architecture.<sup>7</sup> At high porosity, tissues more resemble a granular packing, which is mechanically characterized by a heterogeneous and anisotropic stress distribution.<sup>8,9</sup> Experimental measurements of *in situ* mechanical stress in tissue spheroids have revealed the existence of large heterogeneity and radial anisotropy in mechanical stress.<sup>10–13</sup> It is not known to what extent this heterogeneity and radial anisotropy result from different mechanical properties at the sub-cellular scale, and to what extent they can be explained from the shape and topology of the cells as they accommodate the spherical tissue geometry. Similarly, it remains to be understood how measurable mechanical properties of single cells, through the establishment of tissue microstructure, determine the appropriate parameterization of mechanical stress at the tissue scale.

In this work, we quantify mechanical stress in structurally heterogeneous tissue spheroids using a computational modeling approach. Virtual tissue spheroids are generated using a Deformable Cell Model (DCM). The DCM simulates the visco-elastic deformation of the cell cortex and formulates explicit contact forces to model adhesive interactions between cells.<sup>14,15</sup> Similar to vertex models, it is tuned using a small set of experimentally accessible mechanical parameters such as interfacial tension and active tension.<sup>16</sup> At the same time, its contact-centered implementation allows for the simulation of

<sup>a</sup> MeBioS, KU Leuven, Heverlee, Belgium. E-mail: Maxim.Cuvelier@kuleuven.be

<sup>b</sup> Prometheus, Division of Skeletal Tissue Engineering, KU Leuven, Leuven, Belgium

<sup>c</sup> Team MAMBA, Inria de Paris, Paris, France

<sup>d</sup> Institute of Chemical Engineering Sciences (ICEHT), Foundation for Research and Technology – Hellas (FORTH), Patras, Greece

<sup>e</sup> Skeletal Biology and Engineering Research Center, Department of Development and Regeneration, KU Leuven, Leuven, Belgium



loose cell packing, dynamic cell rearrangements and the open boundaries that typify early stage cell aggregates. As such, it bridges the gap between two limiting tissue descriptions: granular packing in the colloidal limit and fully confluent tissues in the adhesive limit.<sup>17</sup> Based on DCM simulations, we quantify how the distribution and propagation of mechanical stress in various microstructural configurations relates to theoretical models of granular assemblies and homogeneous visco-elastic materials.

## Methods

### Mechanical model

Cells are approximated as visco-elastic and contractile shells that surround a near-incompressible cytoplasm. Mechanically, the shell represents the acto-myosin cortex, which is parameterized by its Young's modulus  $E$ , Poisson's ratio  $\nu$ , thickness  $t$ , viscosity  $\eta$  and active tension  $\gamma$ .<sup>14</sup> We assume that the force-deformation response of a single cell is dominated by the acto-myosin cortex. Cell-cell interactions are implemented by means of a fixed uniform adhesive tension  $\omega$  on the surface of the shells,<sup>15</sup> see Fig. 1. This effective adhesive tension defines the work needed to separate a pair of adhering cells and can be estimated from pull-off force experiments.<sup>18</sup> It should be noted that  $\omega$  also incorporates the reduction of active cortical tension at cell-cell contacts, and may be significantly larger than the total binding energy density of adhesion molecules shared by an adhering pair, see Appendix A.<sup>19,20</sup>

Computationally, the mechanical model of a single cell is implemented as a triangulated surface mesh, representing the acto-myosin cortex. The node positions in this network represent the degrees of freedom in our system and govern how the cells deform and interact.<sup>9,14,15</sup> The motion of these nodes is governed by a system of overdamped equations

$$\mathbf{F}_i(\{\mathbf{x}_j\}) = \sum_j \Gamma_{ij} \cdot \mathbf{v}_j, \quad (1)$$

where conservative forces  $\mathbf{F}_i$  on individual nodes are balanced by dissipative forces determined by a friction matrix  $\Gamma_{ij}$ . The conservative forces on a given node  $\mathbf{F}_i$  incorporate both the mechanics of a single cell as well as inter-cellular contact mechanics, in particular

$$\mathbf{F}_i(\{\mathbf{x}_j\}) = \sum_j \mathbf{F}_{ij}^{\text{el}} + \sum_{(AB):i \in A} \mathbf{F}_{AB,i}^{\text{bend}} + \mathbf{F}_i^{\text{act}} + \mathbf{F}_i^{\text{cyt}} + \sum_{(AB):i \in A} \mathbf{F}_{AB,i}^{\text{adh}},$$

where  $\mathbf{F}^{\text{el}}$  represent an in-plane cortex elasticity, cf. (8), while  $\mathbf{F}^{\text{bend}}$  describe cortex bending rigidity (10),  $\mathbf{F}^{\text{act}}$  originates from an active cortical tension (11),  $\mathbf{F}^{\text{cyt}}$  is a cytosolic response (13) and  $\mathbf{F}^{\text{adh}}$  is adhesion between multiple cells (7).  $\Gamma_{ij}$  can similarly be deconstructed into contact friction  $\Gamma_{AB}^{\text{fric}}$ , cf. (18), cortical friction  $\Gamma_{ij}^{\text{c}}$  due to cortex viscosity, cf. (16), and Stokes drag  $\Gamma_{ii}^{\text{f}}$  representing friction of the surrounding fluid, cf. (14). Due to the non-trivial weighting of these different contributions, we refer to the Appendix A for a more in-depth description.

The generated virtual tissue spheroids are relaxed over time by solving eqn (1) for  $\mathbf{v}_i$  and integrating the nodal positions

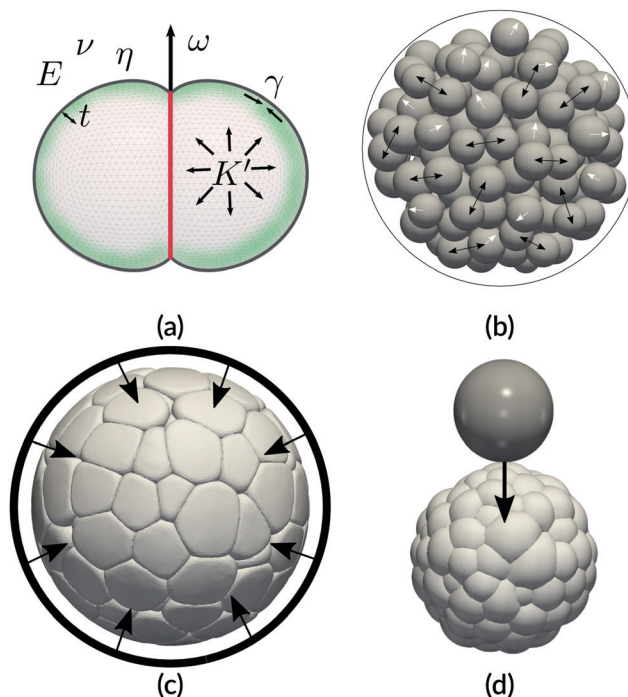


Fig. 1 Mechanical model and simulation setups. (a) Schematic representation of a pair of adhering cells. Triangulated surface meshes are used to represent visco-elastic cortical shells with thickness  $t$ . Passive mechanical properties (Young's modulus  $E$ , Poisson ratio  $\nu$  and viscosity  $\eta$ ) and active mechanics (contractility  $\gamma$  and apparent bulk modulus  $K'$ ) are illustrated in the left and right cell respectively. Contact mechanics are based on a linear contact model with adhesive tension  $\omega$ . (b) Simulated annealing procedure. Black arrows represent cell-cell repulsive potentials while white arrows represent random forces. Initially, the random forces dominate the system. As the annealing simulation progresses, the magnitude of random forces decrease and potential forces increase until an (non-thermal) equilibrium is reached. (c) Snapshot of a DCM aggregation simulation during the tissue compaction step. Spheroids are initialized with the compact granular piles from the annealing procedure and are briefly compressed before being allowed to find a new equilibrium. The compression step was added to unjam the granular piles. (d) Simulated confined indentation experiments are performed to mechanically probe the spheroids. A spherical bead with radius  $3R^{\text{cell}}$  applies a constant force of 15 nN on the tissues.

accordingly. A detailed description of the computational model, including expressions for the individual force contributions is provided in Appendix A.

Within the simulated virtual tissue spheroids, we compute three mechanical measures, each related to distinct biological mechanisms of mechanosensing:

(1) The planar stress in the cortex-membrane complex, which affects tension sensing machinery of the cell such as stretch-activated membrane channels,<sup>21</sup> is parameterized by the in-plane net surface tension

$$\gamma^{\text{eff}} = \frac{1}{2} \text{Tr} \sigma^{\text{p}}, \quad (2)$$

with  $\sigma^{\text{p}}$  the planar stress in the two-dimensional cortical sheet.

(2) The mechanical stress at cell-cell junctions, which affects various mechanosensing pathways associated to



cadherin complexes,<sup>22</sup> is parameterized by the normal contact stress  $\sigma_{nm}^c$ ,

$$\sigma_{nm}^c = \hat{n} \cdot \sigma^c \cdot \hat{n}, \quad (3)$$

where  $\sigma^c$  is the contact stress and  $\hat{n}$  is the normal direction on the cell surface.

(3) The average mechanical stress inside the cell, associated to nucleus mechanotransduction pathways such as YAP/TAZ, and affects mechanisms that control cell volume,<sup>23,24</sup> is estimated by a measure of the hydrostatic stress  $\sigma^h$  (derivation provided in Appendix B),

$$\sigma_\alpha^h = \frac{1}{3V_\alpha} \oint_{S_\alpha} dS_\alpha(\mathbf{x}) \cdot (\mathbf{x} - \mathbf{x}_\alpha) P_\alpha^{\text{adh}}(\mathbf{x}) \quad (4)$$

where  $\mathbf{x}_\alpha$ ,  $S_\alpha$ ,  $V_\alpha$  and  $P_\alpha^{\text{adh}}$  are the center, surface, volume and contact pressure on the cell surface of a cell  $\alpha$ .

The computational approximation of these mechanical measures, in a virtual tissue spheroid generated using the DCM, is detailed in Appendix C.

### Simulation procedure

Our simulation setups consist of a seeding, aggregation and loading phase. During seeding, stiff non-adherent beads are randomly generated in a target volume and a simulated annealing procedure<sup>25</sup> is used to generate compact granular piles, see Fig. 1b and Appendix E. Bead sizes are polydisperse and sampled from a gamma distribution with shape parameter  $k \approx 37.75$  and scale parameter  $\theta \approx 0.24$ , based on experimental data from Smeets *et al.*<sup>9</sup>

Next, beads are replaced with deformable cells with corresponding positions and radii. During aggregation simulations, cells are initially compacted until a confluent state is reached. The confining pressure is released, allowing the system to relax until a new (local) energetic minimum state is found, see Fig. 1c. Mechanical measures are extracted, before starting the loading phase.

In the final phase, spheroids are subjected to a confined indentation simulation to quantify how mechanical loads

propagate through the tissue, see Fig. 1d and Appendix G. Similar to the unloaded tissues, mechanical measures are extracted once the system reaches a steady-state. For each configuration, which requires a computation time of  $\approx 80$  h we performed five independent replicates per setup and pool the data per configuration.

## Results

### Heterogeneity and anisotropy of mechanical stress

Simulations of spheroids were performed using the DCM to assess the spatial distribution of mechanical stress. Fig. 2 shows a comparison of simulated spheroids between reference conditions (Table 1, A), cells with decreased adhesion strength (B) and cells with decreased cortical stiffness (C). With decreased adhesion, a loose granular aggregate is observed, whereas a decrease in cortical stiffness results in compact, nearly confluent micro-tissues. In all three conditions, the mechanical measures  $\gamma^{\text{eff}}$ ,  $\sigma_{nm}^c$  and  $\sigma^h$  are spatially heterogeneous across the spheroids, indicating a large variance of the mechanical microenvironment between individual cells. Moreover, a distinct radial anisotropy separates the core from the periphery. The effective surface tension is highly tensile at the periphery and lower at the inner surface of the periphery (Fig. 2b). Intermediate tensions are observed at the core. Cell-cell junctions between peripheral cells are under tensile stress (Fig. 2c), while the average junction stress at the core is lower. The average intercellular stress is tensile towards the periphery of the spheroid (Fig. 2d). These conditions parallel the apico-basal asymmetry and mechanical state of a typical epithelium.<sup>26</sup> Conversely, cells in the core are compressed and display a large variance in cortical tension and intercellular stress. Inter-cellular variation in mechanical conditions are caused by the granular nature of the spheroid, whereas further inter-cellular variation results from microscopic pores near triple junctions, which demonstrate elevated levels of tensile stress.

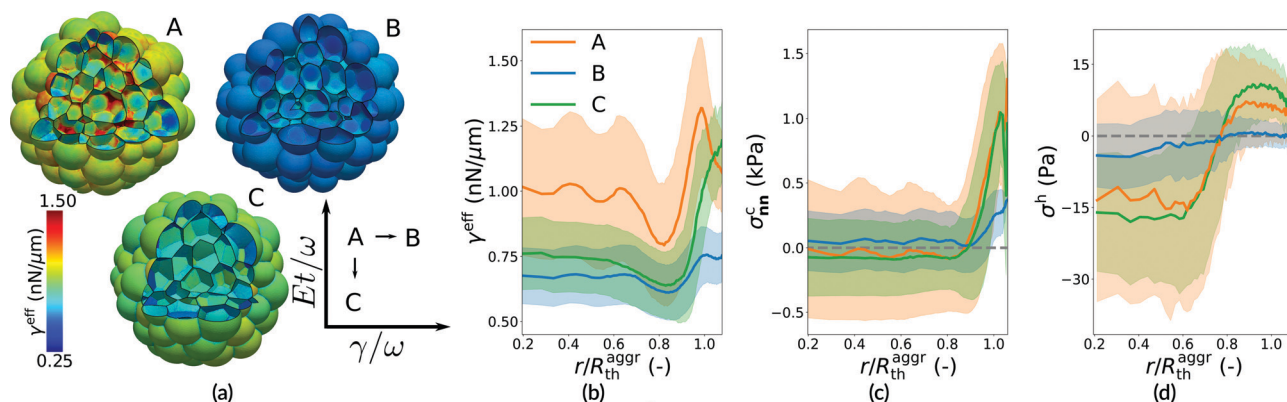


**Fig. 2** Heterogeneity and anisotropy of stress distribution (a) simulation snapshot of three setups: reference case A, case B decreased adhesion strength and case C decreased cortical stiffness, using dimensionless parameters  $\gamma/\omega$  and  $Et/\omega$ . (b) Distribution of mean  $\gamma^{\text{eff}}$  with standard deviation over the normalized radial positions  $r/R_{\text{th}}^{\text{aggr}}$ . (c) Radial distribution of contact pressures  $\sigma_{nm}^c$ . (d) Radial profile of the hydrostatic stress  $\sigma^h$ . All cases exhibit a compressed core and tensile periphery.



Table 1 Reference table of simulated cell mechanical properties

Parameter	Symbol	Case A	Case B	Case C	Units	Source
Mean cell radius	$R^{\text{cell}}$	9.0			$\mu\text{m}$	9
Effective cortical thickness	$t$	200			nm	15, 27 and 28
Cortical stiffness	$E$	20	5	0.3125	kPa	15 and 27
Poisson's ratio cortex	$\nu$	1/3			—	29
Cortical tension	$\gamma$	0.5			$\text{nN } \mu\text{m}^{-1}$	15, 27, 30 and 31
Adhesive tension	$\omega$	0.5	0.125	0.5	$\text{nN } \mu\text{m}^{-1}$	19
Cell count	$N$	150			—	

To put these results in context of experimental findings, we first compare the distribution of  $\sigma_{nn}^c$  on the surface of individual cells to experimental measurements of cell-generated stress using *in situ* pressure probes. In growing undifferentiated melanoma tumor-repopulating cell colonies, Mohagheghain *et al.* observe a heterogeneous distribution of normal and shear stresses in the range of  $-358$  Pa and  $49$  Pa respectively.<sup>32</sup> For reference case A, we obtain comparable values (Fig. 3b and c). Unlike on our ‘virtual cells’, Fig. 3a, Mohagheghain *et al.* did not observe any tensile stress on their pressure probes, possibly due to the use of encapsulating hydrogels that favor a global compressed state in the spheroid, or due to the reduced adhesive tension in passive pressure probes. Still, our simulations indicate that the existence of a radial gradient combined with the granular micro-architecture inside of the spheroid are sufficient to explain the overall observed heterogeneity of mechanical stress. For comparison to the work of Campàs *et al.*, we compute the “maximum anisotropic stress”, defining it as the difference between 95th and 5th percentile of  $\sigma_{nn}^c$  per cell.<sup>10</sup> We find values in the measured range between  $1.5$  kPa and  $3.6$  kPa, see Fig. 3d. Changing mechanical properties (A, B, C) has a strong influence on the estimated maximum anisotropic stress, which is in line with the observations when changing the cell type. In a follow-up study, Lucio *et al.* computed the “Mean anisotropic stress” as the standard deviation of the stress distribution per cell.<sup>12</sup> In contrast to our observations when computing this measure, Fig. 3e, they found no significant radial asymmetry. However, in

our simulations, the mean anisotropic stress is only elevated in the outer cell layer, whereas no pressure sensors were observed in the outer cell layers in the study of Lucio *et al.*

### Applicability of liquid droplet force balance

The observed radial dependency of the mean normal stress (Fig. 3c) hints at the existence of a non-uniform bulk tissue pressure, which is measured by the hydrostatic pressure  $\sigma^h$ . In analogy to liquid droplets, the Young–Laplace equation is commonly used to describe the relation between tissue surface tension and the pressure drop across its interface.<sup>33</sup> Given our observations, the apparent surface tension of the tissue is established by the adhesive tension  $\omega$ , similar to the cohesion energy between the constituent elements of an isotropic material, see Appendix F.<sup>34,35</sup> Hence, given the minimal confluent spheroid

radius  $R_{\text{th}}^{\text{aggr}} = \sqrt[3]{\frac{3}{4\pi} \sum_x V_x}$ , the theoretical pressure drop over the interface is

$$\sigma_{\text{th}}^h = 2\omega/R_{\text{th}}^{\text{aggr}}. \quad (5)$$

Fig. 4 shows how the local hydrostatic stress  $\sigma_x^h$  in simulations compares to  $\sigma_{\text{th}}^h$  for varying cell mechanical properties. Fixing  $Et/\omega = 1/8$  and decreasing results in spheroids with an increasingly tensile periphery, and a compressed core in which  $\sigma_x^h$  converges to  $\sigma_{\text{th}}^h$  (Fig. 4a). The same trend can be observed when fixing  $\gamma/\omega = 1/2$  while decreasing  $Et/\omega$ . However, at high

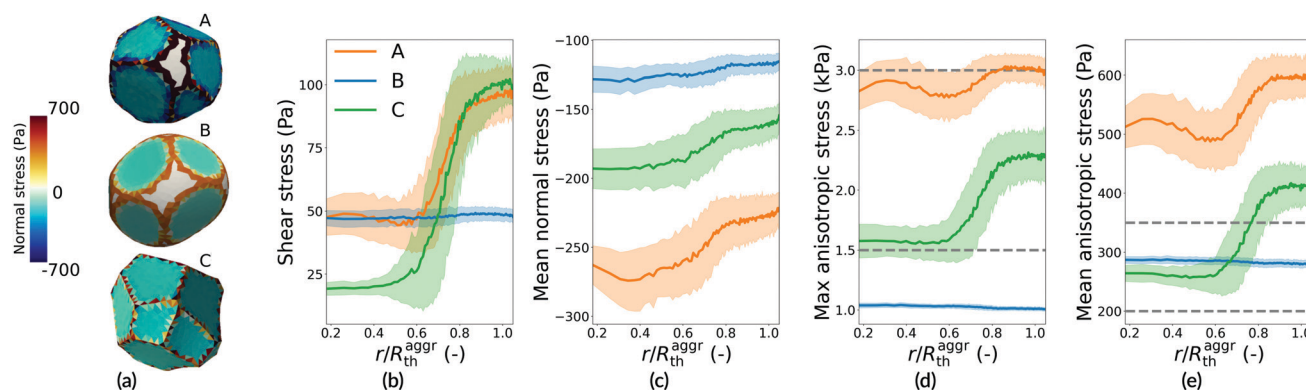
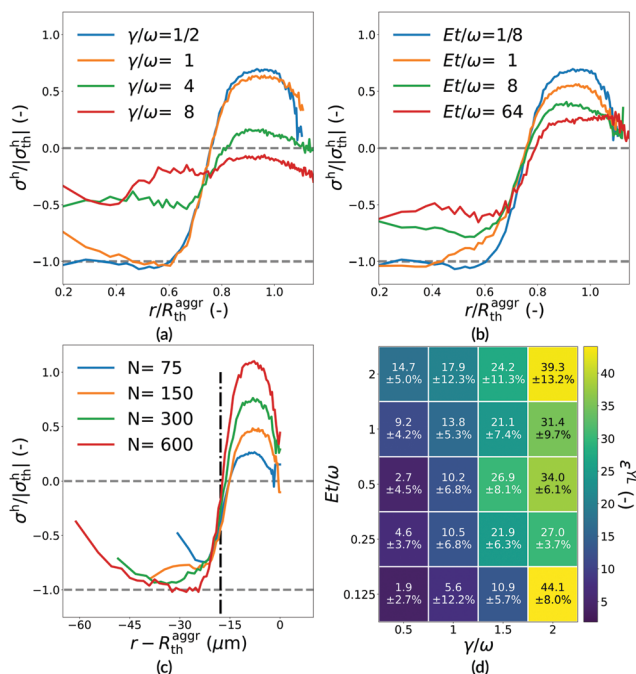


Fig. 3 Comparison to experimental data (a) visualization of normal stress  $\sigma_{nn}^c = \hat{n} \cdot \sigma^c \cdot \hat{n}$  on a simulated cell inside of the virtual tissue. (b) Radial distribution of mean shear stress  $|\sigma^c \cdot \hat{n} - (\hat{n} \cdot \sigma^c \cdot \hat{n}) \hat{n}|$  per cell. (c) Radial distribution of the mean normal stress  $\sigma_{nn}^c$  per cell. (d) Radial distribution of maximal anisotropic stress, calculated as the difference between the 95th and 5th percentile of  $\sigma_{nn}^c$  acting on an individual cell. Experimentally measured limits of  $1.5$  kPa and  $3.6$  kPa are represented by the grey dotted lines.<sup>10</sup> (e) Radial profile of the mean anisotropic stress  $\text{std}(\rho(\sigma_{nn}^c))$  acting on an individual cell. Experimentally measured limits of  $200$  Pa and  $350$  Pa are represented by the grey dotted lines.<sup>12</sup>







**Fig. 4** Comparison to liquid droplet mechanics (a and b) normalized  $\sigma^h$  over normalized radial positions while fixing  $Et/\omega = 1/8$  or  $\gamma/\omega = 1/2$  respectively. For  $\omega$  dominated systems,  $\sigma^h$  approaches the tissue-scale Young–Laplace pressure  $\sigma^h_{th}$  in the core. (c) Varying the amount of cells in a spheroid reveals the absolute scaling of the width of the tensile periphery. The black vertical line denotes the transition from a contractile to a compressed state, which occurs at the depth of one cell diameter. Peak tension is observed at a depth of one cell radius. (d) Heat map of relative difference  $\varepsilon^{YL}$  in % for different setups. Decreasing adhesion (increasing  $\gamma/\omega$ ) results in a steady increase of  $\varepsilon^{YL}$  until the continuum approximation breaks down and  $\varepsilon^{YL}$  varies wildly. Increasing stiffness  $Et/\omega$  has a similar, but less pronounced effect.

$\gamma/\omega$ , the simulated spheroids fail to establish a periphery that is sufficiently well connected to generate a net surface tension and the clear distinction between cells in the core and at the periphery breaks down (Fig. 4b).

To determine how the relative size of tensile and compressed regions changes with spheroid size, we performed simulations with varying cell counts, Fig. 4c. These demonstrate that the thickness of the tensile periphery does not scale with the total spheroid size, but remains constant and roughly corresponds to one cell diameter. Similarly, the peak in tensile stress occurs at a distance of one cell radius from the outer surface. This observation is consistent with the liquid droplet model, in which a microscopically thin tensile layer envelops a continuous isotropic compressed core. A notable discrepancy with liquid theory is that the magnitude of hydrostatic stress decreases towards the spheroid center. We propose that this behavior can be attributed to mechanical shielding effects, as the granular architecture of the spheroids allows for the formation of force bridges that shield underlying cells from compressive loads. Indeed, as the spheroid structure becomes confluent with increasing adhesion, this effect disappears and a clear plateau in  $\sigma^h$  is observed, Fig. 4b.

To quantify the accordance to liquid theory, we calculate the mean hydrostatic stress  $\langle \sigma^h \rangle$  for all cells with a radial position  $r < R^{\text{aggr}}_{th} - 2R^{\text{cell}}$ . From this, we define the relative error  $\varepsilon^{YL} = 1 - \langle \sigma^h \rangle / \sigma^h_{th}$  as a measure for the applicability of the Young–Laplace law. Fig. 4d shows that for sufficiently large values of cell–cell adhesion, the Young–Laplace law provides a good approximation of the global mechanical balance in the spheroid.

### Distribution and propagation of external forces

Tissues are frequently subjected to external loads which alter the self-established microenvironment of constituent cells. We investigated the distribution of mechanical forces in a simulated mechanical loading experiment. For this, simulated spheroids were confined by a convex hull before being subjected to a load of 15 nN, applied by a spherical probe with radius  $3R^{\text{cell}}$ , see Appendix G. Cell–cell connectivity and the distribution of normalized cell–cell contact normal forces

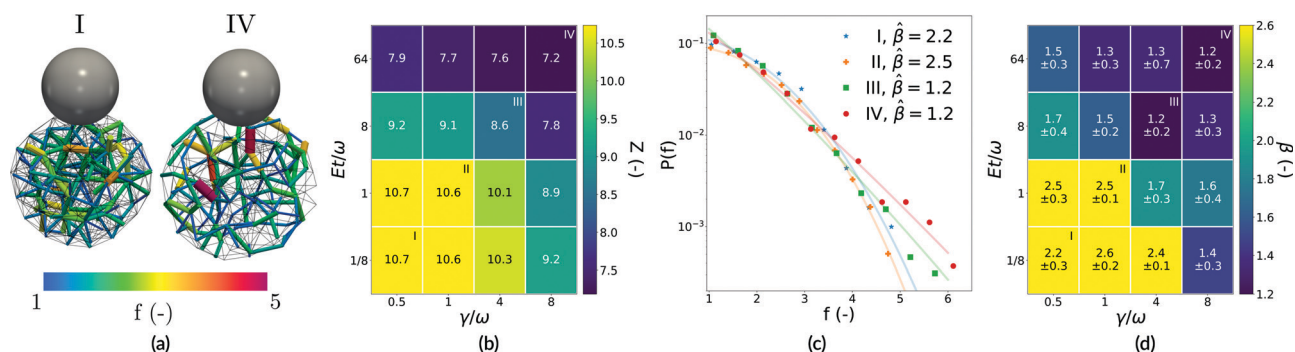


**Fig. 5** Force distribution upon mechanical indentation (a) cell–cell connectivity graph where nodes (cells) are connected with weighted edges, representing normalized contact forces  $f$ . In the soft adhesive case I, the graph is well connected and  $f$  is distributed fairly homogeneous. Tissues consisting of stiff non-adherent cells, case IV, form less connected graphs where the distribution of  $f$  appears more anisotropic. (b) Heat map of mean coordination number  $Z$  for the different simulated setups. For soft adhesive cases,  $Z$  is saturated at  $\approx 10.6$ – $10.7$ . As  $Et/\omega$  and  $\gamma/\omega$  increase,  $Z$  decreases; reflecting the decrease in graph connectivity. (c) Estimated probability distribution of  $f$  with estimated exponent  $\beta$  for  $P(f) \propto \exp(-f^\beta)$ . For the fit of  $\beta$ , only  $f > 1$  data was used. Bin widths and counts were determined by using Doane's formula, taking into account the skewness of the data. (d) Heat map of  $\beta$  for different setups. For tissues consisting of stiff non-adhesive cells,  $\beta$  approaches unity. As adhesion increases or cell stiffness is decreased,  $\beta$  increases before reaching a plateau at  $\approx 2$ – $2.5$ .

$f = -F^c / \langle F6c \rangle$  were extracted, with  $\langle F^c \rangle$  as the mean magnitude of contact normal forces in the system. Fig. 5a visualizes the contact force distribution throughout the tissue, using a network representation of the tissue with cells as nodes and cell-cell contacts as edges. Tissues consisting of soft adhesive cells (Fig. 5a left) exhibit a higher connectivity than tissues consisting of stiff non-adherent cells (Fig. 5a right). This difference in connectivity is reflected in the mean coordination number  $Z$ , see Fig. 5b. In granular piles, a value of  $Z$  close to the critical coordination number  $Z_c$  is linked to the presence of force chains in the system.<sup>†</sup> These pronounced force chains are responsible for the highly anisotropic propagation of loads. Given the accordance to granular theory, as  $Z$  increases, loads are distributed increasingly even as the network connectivity improves.<sup>8</sup> Apart from tissue connectivity we also analyzed the scaling of the probability density function of contact forces  $P(f)$  between different configurations, see Fig. 5c. In the limit of granular particles, an exponential decay is expected, where high contact forces are increasingly rare  $P(f) \propto \exp(-f)$ . As the spheroids become progressively compressible, the expected scaling approaches the normal distribution  $P(f) \propto \exp(-f^2)$  as forces are more evenly distributed in the network.<sup>8</sup> In order to locate the simulated spheroids in this range, we fit  $P(f) \propto \exp(-f^\beta)$ , estimating  $\beta$  by using an unconstrained curve fitting procedure, see Fig. 5d. We observe a transition from  $\beta \approx 2$  to  $\beta \approx 1$  as adhesion decreased or as cortical stiffness increased.

## Discussion

In this work, we presented a mechanical model of multi-cellular tissue spheroids that takes into account the microscopic structure of the cellular material. The distribution and propagation of mechanical forces inside virtual tissue spheroids were quantified and compared to experimental measurements and theoretical limits. For a reference configuration based on typical cell-like mechanical properties, we obtain similar estimates for the magnitude and heterogeneity of shear and normal stress measures as experimentally measured.<sup>10,12,32</sup>

Simulations revealed an inherent core-periphery asymmetry established by the force-balance at the tissue boundary. We demonstrated that in the limit of soft and adhesive cells, this asymmetry can be well approximated using the model of a liquid droplet, which balances the tissue's internal pressure with surface tension at the periphery. The asymmetry between cells in the core and at the periphery is reflected in the properties of the mechanical microenvironment, and is established even in absence of mechanical heterogeneity in the underlying cell population. This is of importance in the context of micro-tissues, since no prior biochemical gradient is required to establish this asymmetry. At the same time, cells experience different mechanical conditions depending on their location in the spheroid: cells at the periphery are under

pronounced lateral tension that is reminiscent of the mechanical state of an epithelium, whereas cells at the core are generally under compression, of which the magnitude and heterogeneity depend on cell mechanical properties. Eventually, mechanotransduction pathways may consolidate these differences in discrepancies in cell fate.<sup>36</sup> For example, we observed that for larger spheroids, the relative size of the peripheral region decreases, and shielding effects may decrease compression at the core. Hence, it could be expected that the altered distribution of mechanical states results in a different composition of cell types, even in absence of mass transport effects.<sup>37,38</sup> Recent experiments support this notion.<sup>39</sup> However, given the limitations of our model and current experimental techniques, more data is still needed to validate this claim.

Finally, we showed that two regimes of force distribution occur, depending on the loading conditions and cell mechanical properties: stiff granular spheroids exhibit force bridges and highly heterogeneous force distributions, whereas soft, adhesive and confluent tissues behave like a compressible granular material with a normal distribution of internal mechanical forces. In the stiff granular regime, the heterogeneity in the mechanical microenvironment may be very large, even for adjacent cells. As such, in absence of other control mechanisms, mechanotransduction processes could amplify heterogeneity in cell fate for spheroids in these configurations. Loaded conditions on small multicellular assemblies are common in many biological applications, for example in growing spheroids encapsulated in elastic materials.<sup>40,41</sup> Hence, it may be opportune to identify the loading regime, which is reflected in the microscopic architecture of the cellular packing through the cell-cell connectivity number.

This work approximated cellular properties based on a mechanical description that focuses on the cell cortex. Comparing to realistic cells, this approach has some evident limitations, the implication of which will be discussed here. First of all, we assumed cellular properties to be static over time, whereas in reality, many cellular properties are dynamic, responsive, and often timescale dependent.<sup>33</sup> Moreover, by not including active motility, simulated cells are effectively frozen in a jammed state. These limitations prevent us from analyzing tissue rheology and dynamics. Still, in many biological systems, both *in vivo* and *in vitro*, cells are not very motile, and remain in a jammed configuration.<sup>42</sup> Secondly, our model considers mechanical properties to be uniform across the cell. For example, we assumed constant non-specific adhesive tension. In reality, adhesive ligands tend to be strongly clustered near the edges of cell-cell contacts, a phenomenon that could alter the distribution of inter-cellular stress.<sup>43</sup> However, the modeled 'adhesive tension', expressed in the force balance at an inter-cellular junction, stems from the combination of adhesion energy and differential interfacial tension, see Appendix A. The latter originates from a decrease of acto-myosin contractility near cell-cell interfaces and has been shown to dominate the energy contribution in the net adhesive tension.<sup>19,20,44</sup>

Finally, our model does not take into account the presence of extracellular matrix, which is expected to contribute heavily

<sup>†</sup> The specific value of  $Z_c$  is determined by the dimensionality of the system and the relative contribution of contact friction; for our setups we estimated  $Z_c \approx 6$ , given the low contact friction in the simulated setups.



to force transmission and distribution. This limits the applicability of the model predictions to immature artificial spheroids and early developmental structures, where the pericellular matrix is absent or sufficiently thin to justify its exclusion.<sup>45</sup> Future developments that take into account the contribution of the aforementioned phenomena in a similar modeling strategy will allow the quantification of mechanical effects due to tissue dynamics, and of changes in the mechanical microenvironment during tissue maturation.

## Author contributions

M. C., H. R. and B. S. conceived the project. M. C. and B. S. designed and conducted the simulations, M. C., J. P. and B. S. performed data analysis. M. C., J. P., I. P. and B. S. wrote the manuscript. All authors commented on the manuscript.

## Conflicts of interest

There are no conflicts to declare.

## Appendix A: deformable cell model

The acto-myosin cortex of a cell is represented by a visco-elastic shell. We approximate this shell by a triangulated surface mesh with effective thickness  $t$ , and nodal positions  $\mathbf{x}_i$  as the relevant degrees of freedom. First, contact mechanics are briefly summarized, after which implementation of the visco-elastic cortical shell model is discussed.

### Contact mechanics

In the mechanical cell model, we assume a fixed and uniform adhesive tension  $\omega$  across the cell surface. The adhesive tension incorporates cell-cell adhesive interactions as well as the effect of cortical tension reduction at the cell-cell interface:  $\omega_A = \omega^{\text{int}} + \gamma - \gamma^i$ , where  $\omega^{\text{int}} [\text{J m}^{-2}]$  represents the adhesive energy density due to adhesion molecule interactions and depletion forces at the interface,  $\gamma [\text{N m}^{-1}]$  is the cortical tension or equivalently the cell-medium interfacial tension and  $\gamma^i [\text{N m}^{-1}]$  is the cell-cell interfacial tension.<sup>19,20,40</sup> The total adhesive tension  $\omega$  acting on interface (AB) is given by  $\omega = \omega_A + \omega_B$ .

A linear force, scaling with contact overlap  $\delta$ , was introduced to represent repulsive interactions between surfaces and ensure stable contacts. The contact potential for contact-pair (AB) with contact area  $S_{AB}$  is then given by

$$E_{AB}^{\text{adh}} = \left( \frac{\delta_{AB}}{h_0} - \frac{\delta_{AB}^2}{2h_0^2} \right) \omega S_{AB}$$

where a distinction can be made between the attractive and repulsive energy contributions respectively. The effective range of adhesion  $h_0$  was incorporated by virtually translating contact surfaces along their normals, see Fig. 6. Contact overlap distance  $\delta_{AB}$  is calculated with respect to these translated surfaces.

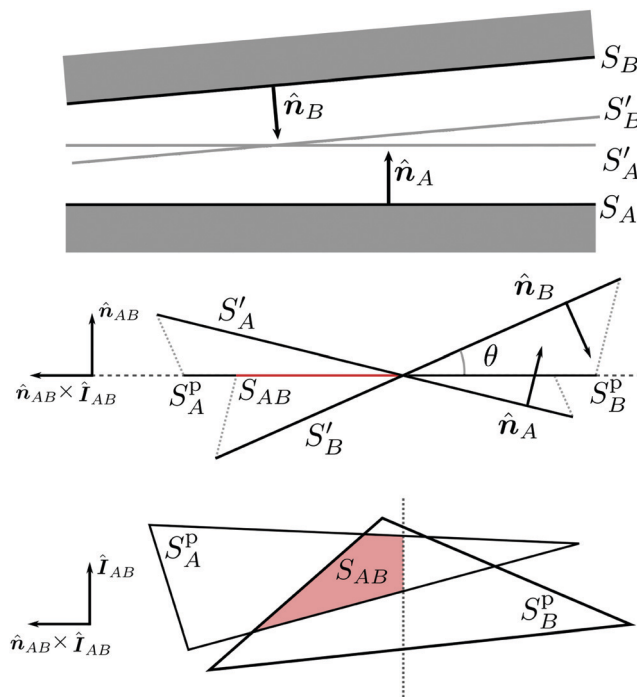


Fig. 6 Contact geometry: (top) side view of surfaces A and B. To compute the overlap distance, the surfaces are virtually translated for the range of adhesion  $h_0$  along their normals. Contact model calculations are then performed based on the translated surfaces  $A'$  and  $B'$ . (mid) Side view according to the direction of the intersection line  $\hat{l}_{AB}$  for translated triangle pair ( $A'$ ,  $B'$ ). The dotted horizontal line represents the contact plane, the smaller dotted lines represent the direction in which the triangle areas are projected on the plane. The red line segment represents the contact polygon  $A \cap B$ , the intersect of projected triangles  $A^p$  and  $B^p$  is represented by  $S_{AB}$ . Contact angle  $\alpha$  is estimated as  $\cos(\theta) = \hat{n}_{AB} \cdot \hat{n}_A$ . (bottom) Top view according to contact normal  $\hat{n}_{AB}$  for intersecting triangle pair ( $A'$ ,  $B'$ ). The dotted vertical line represents the intersection line  $\hat{l}_{AB}$ . Projected areas  $S^p$  are defined by projecting triangle areas  $S$  via the normal direction of their intersection partner on the contact plane.

The resulting contact pressure  $P_{AB}^{\text{adh}}$  is estimated with a linear contact pressure model where no energy is stored in deformation at equilibrium

$$P_{AB}^{\text{adh}}(\mathbf{x}) = k_{AB} \delta_{AB}(\mathbf{x}) - P_{AB}^0,$$

contact stiffness  $k_{AB}$  and adhesive pressure  $P_{AB}^0$  need to be set. To ensure that at equilibrium ( $P_{AB}^{\text{adh}} \equiv 0$ ) the work of adhesion  $\omega$  is recovered, contact stiffness has to be defined as  $k_{AB} = P_{AB}^0/h_0$  with  $P_{AB}^0 = \omega/h_0$ . The specific value  $h_0$  does not influence simulation outcome due to the scale separation,  $h_0 \ll R^{\text{cell}}$ . This is valid for all performed simulations as the effective range of adhesion  $h_0$  was estimated as 300 nm.<sup>46</sup> Contact overlap distance at point  $\mathbf{x}$  was defined as

$$\delta_{AB}(\mathbf{x}) = \max\{0; 2(\mathbf{x} - \mathbf{s}_{AB}) \cdot (\hat{n}_{AB} \times \hat{l}_{AB}) \tan \theta\},$$

where  $\theta$  is the contact angle,  $\hat{n}_{AB} \propto (\hat{n}_B - \hat{n}_A) \times \hat{l}_{AB}$  the contact normal and  $\mathbf{s}_{AB}$  is an arbitrary point on the intersection line defined by  $\hat{l}_{AB} \propto \hat{n}_A \times \hat{n}_B$ , as reported by Smeets *et al.*,<sup>47</sup> see also Fig. 6. The resulting contact forces and moment are obtained by integrating the total contact pressure over the oriented contact



area  $S_{AB}$ ,

$$\mathbf{F}_{AB}^{\text{adh}} = \int dS_{AB}(\mathbf{x}) P_{AB}^{\text{adh}}(\mathbf{x}). \quad (6)$$

To distribute the contact forces acting on the contact plains to the nodal contact forces  $\mathbf{F}_{AB,i}^{\text{adh}}$ , it is assumed that the nodal forces are collinear with the contact normal  $\hat{\mathbf{n}}_{AB}$ . This results in a system of linear equations per contact pair  $(AB)$

$$\begin{aligned} \sum_{i \in A} \mathbf{F}_{AB,i}^{\text{adh}} &= - \int_{x \in A \cap B} dS_{AB}(\mathbf{x}) P_{AB}^{\text{adh}}(\mathbf{x}) \\ &\times \sum_{i \in A} [(\|\hat{\mathbf{n}}_{AB} \otimes \hat{\mathbf{n}}_{AB}\) \cdot (\mathbf{x}_i - \mathbf{x}_{AB})] \times \mathbf{F}_{AB,i}^{\text{adh}} \quad (7) \\ &= \int_{x \in A \cap B} dS_{AB}(\mathbf{x}) \times (\mathbf{x} - \mathbf{x}_{AB}) P_{AB}^{\text{adh}}(\mathbf{x}) \end{aligned}$$

which guarantees a unique solution for every  $\mathbf{F}_{AB,i}^{\text{adh}}$ . Contact point  $\mathbf{x}_{AB}$  is defined as the geometric center of the intersection polygon  $A \cap B$ .<sup>47</sup> The integrals on RHS are calculated by using a numerical quadrature rule presented in ref. 48 with quadrature points covering each triangle of the triangulated intersection polygon  $A \cap B$  obtained as an intersection of projected triangles on a common plane, see Fig. 6. The solution for this system is presented and discussed in the work of Smeets *et al.*<sup>47</sup>

### Cortex elasticity

Passive mechanical properties dominate cortex behavior at short time-scales ( $< 5$  min). As cortex deformation is assumed to be small, a linear elastic model is used to capture in-plane stretching and compression energy. For nodes  $(ij)$  this gives

$$E_{ij}^{\text{el}} = -k^{\text{el}} \frac{(d_{ij} - d_{ij}^*)^2}{2}$$

where  $d_{ij} = \|\mathbf{x}_j - \mathbf{x}_i\|$  and  $d_{ij}^*$  represent the current and equilibrium distance between nodes  $i$  and  $j$  with positions  $\mathbf{x}_i$  and  $\mathbf{x}_j$  respectively. The linear spring force between the connected nodes is then given by

$$\mathbf{F}_{ij}^{\text{el}} = k^{\text{el}} (d_{ij} - d_{ij}^*) \hat{\mathbf{t}}_{ij} \quad (8)$$

with

$$\hat{\mathbf{t}}_{ij} = \frac{\mathbf{x}_j - \mathbf{x}_i}{d_{ij}}.$$

The linear spring stiffness  $k^{\text{el}}$ , under our assumption of an isotropic linear elastic material model, can be approximated by using Van Gelder's formula:

$$k^{\text{el}} = \frac{Et(S_{A,ij} + S_{B,ij})}{d_{ij}^{*2}}$$

in which  $(S_{A,ij} + S_{B,ij})$  is the area of the connected triangle pair  $(AB)$  associated with spring  $(ij) \in A \cap B$ .<sup>49</sup>  $E$  and  $t$  are cortex specific parameters, representing the Young's modulus and effective thickness of the cortex.

Due to its non-zero thickness, the cortex also has bending rigidity. The energy required to bend connected triangles  $(AB)$  is

given by

$$E_{AB}^{\text{bend}} = k^{\text{bend}} [1 - \cos(\theta_{AB} - \theta_{AB}^*)] \quad (9)$$

in which  $\theta_{AB}$  and  $\theta_{AB}^*$  represent the instantaneous and spontaneous angles between a pair of adjacent triangles  $(AB)$ . Derived from the macroscopic (continuum) flexural rigidity of a sheet, we estimate

$$k^{\text{bend}} = \frac{Et^3}{12(1 - \nu^2)}$$

with  $\nu$  as the Poisson ratio of the cortex. To be consistent with the assumption of an isotropic linear elastic material,  $\nu$  is fixed at a value of 1/3.<sup>29</sup> The bending force

$$\mathbf{F}_{AB,i}^{\text{bend}} = -\frac{\partial E_{AB}}{\partial \mathbf{x}_i} \quad (10)$$

acting on each of the triangle nodes  $i \in A$  are distributed as derived by Fedosov.<sup>50</sup>

### Active cellular properties

Tension generated in the cortex results from acto-myosin contractility which we represent as an effective surface tension  $\gamma$  in the cortical shell model. Using the derivation of Fedosov *et al.*,<sup>51</sup> the direct force contribution of surface tension  $\gamma$  is given by

$$\mathbf{F}_i^{\text{act}} = \frac{\gamma}{2} (\mathbf{x}_k - \mathbf{x}_j) \times \hat{\mathbf{n}}_A, \quad (11)$$

where  $i, j, k$  are nodes of a single triangle  $A = (ijk)$ .

Since the cytoplasm is assumed to be incompressible, active volume control is implemented *via* a cytoplasmic pressure. We assume the equilibrium volume  $V_\alpha^*$  of a cell  $\alpha$  is constant at short timescales and implemented a proportional-integral-derivative (PID) pressure controller to enforce this. The cytoplasmic pressure  $P_\alpha^{\text{cyt}}(t)$  due to the volume controller is then estimated as

$$P_\alpha^{\text{cyt}}(t) = -K e_\alpha(t) - \frac{K}{T_I} \int_0^t ds e_\alpha(s) - K T_d \frac{de_\alpha(t)}{dt}, \quad (12)$$

for a cell with volumetric strain  $e_\alpha(t) = (V_\alpha(t) - V_\alpha^*)/V_\alpha^*$ .  $T_I$  and  $T_d$  are typically chosen as one order of magnitude larger than the time-resolution with which the system is updated. In the main text Fig. 1 we used  $K'$  to represent the effective bulk modulus of a cell, lumping the different contributions of eqn (12) into a single parameter.

The total pressure acting on a node

$$P_i(t) = \frac{2\gamma}{R_\alpha^{\text{cell}}} + P_\alpha^{\text{cyt}}(t),$$

includes an additional offset pressure  $2\gamma/R_\alpha^{\text{cell}}$  to balance the acto-myosin contractility in the cortex. This ensures cells are in mechanical equilibrium at the start of the simulations. The force acting on node  $i$  due to nodal pressure  $P_i(t)$ , is obtained by integrating over the node associated oriented Voronoi area  $S_i$ . Given the pressure is constant over the cell surface, the force is simply given by





$$\mathbf{F}_i^{\text{cyt}}(t) = \mathbf{S}_i P_i(t). \quad (13)$$

### Dissipative forces

Apart from conservative forces, dissipative forces are considered as well. A general drag force

$$\mathbf{F}_i^{\text{drag}} = -\Gamma_{ii}^{\text{f}} \cdot \mathbf{v}_i,$$

where

$$\Gamma_{ii}^{\text{f}} = \frac{3\eta^{\text{f}}}{2R^{\text{cell}}} S_{ii}, \quad (14)$$

is included to account for the liquid drag between the cells and their medium due to the fluid viscosity  $\eta^{\text{f}}$ . When dealing with arbitrary shapes this approximation is no longer correct. Even though  $\mathbf{F}_i^{\text{drag}}$  is small compared to other dissipative forces, it is still used to improve the stability of the numerical integration scheme as it ensures the resistance matrix is positive definite, see equation of motion.<sup>52</sup>

A much larger contribution to energy dissipation arises from cortex viscosity. The viscous damping force between two connected nodes is given by

$$\mathbf{F}_{ij}^{\text{visc}} = \Gamma_{ij}^{\text{c}} (\mathbf{v}_j - \mathbf{v}_i) \quad (15)$$

with friction elements

$$\Gamma_{ij}^{\text{c}} = \frac{\eta^{\text{c}}}{\sqrt{3}} \mathbb{I} \quad (16)$$

where  $\eta^{\text{c}}$  represents the cortical viscosity and  $\mathbb{I}$  is the second-order identity tensor. This cortical damper works in parallel with the cortical springs defined in eqn (8).

Finally a viscous contact force is included to account for drag between contacting triangles. The contact drag force acting on node  $i$  of triangle  $A$  of the contact pair  $(AB)$

$$\mathbf{F}_{AB,i}^{\text{fric}} = \Gamma_{AB}^{\text{fric}} \cdot \sum_{k \in B} w_{ik}^{AB} (\mathbf{v}_k - \mathbf{v}_i) \quad (17)$$

determined by a friction tensor  $\Gamma_{AB}^{\text{fric}}$  and weights  $w_{ik}^{AB}$  per node  $k$  of the  $B$  triangle.  $w_{ik}^{AB}$  are assumed to scale with the relative contribution of the nodal contact forces to the overall contact force thus

$$w_{ik}^{AB} = \frac{(\mathbf{F}_{AB,i}^{\text{adh}} + \mathbf{F}_{AB,k}^{\text{adh}}) \cdot \hat{\mathbf{n}}_{AB}}{6 \sum_{\forall k \in B} \mathbf{F}_{AB,k}^{\text{adh}} \cdot \hat{\mathbf{n}}_{AB}}$$

is used as an approximation.  $\Gamma_{AB}^{\text{fric}}$  for a given contact area  $S_{AB}$  is estimated as

$$\Gamma_{AB}^{\text{fric}} = S_{AB} [\gamma^{\perp} \hat{\mathbf{n}}_{AB} \otimes \hat{\mathbf{n}}_{AB} + \gamma^{\parallel} (\mathbb{I} - \hat{\mathbf{n}}_{AB} \otimes \hat{\mathbf{n}}_{AB})]$$

with normal and tangential friction coefficients  $\gamma^{\perp}$  and  $\gamma^{\parallel}$  respectively.

Note that (17) can be equivalently formulated as

$$\mathbf{F}_{AB,i}^{\text{fric}} = \sum_{k \in B} \Gamma_{AB,ik}^{\text{fric}} \cdot (\mathbf{v}_k - \mathbf{v}_i)$$

if we denote

$$\Gamma_{AB,ik}^{\text{fric}} = w_{ik}^{AB} \Gamma_{AB}^{\text{fric}}. \quad (18)$$

### Equation of motion

In the overdamped cellular environment, inertial forces may be neglected.<sup>53</sup> Based on the different contributions described above, the force balance for node  $i$  gives

$$\begin{aligned} \sum_j \mathbf{F}_{ij}^{\text{el}} + \sum_{(AB):i \in A} \mathbf{F}_{AB,i}^{\text{bend}} + \mathbf{F}_i^{\text{act}} + \mathbf{F}_i^{\text{cyt}} + \sum_{(AB):i \in A} \mathbf{F}_{AB,i}^{\text{adh}} \\ = \Gamma_{ii}^{\text{f}} \cdot \mathbf{v}_i + \sum_j \Gamma_{ij}^{\text{c}} \cdot (\mathbf{v}_i - \mathbf{v}_j) + \sum_{(AB):i \in A} \sum_{k \in B} \Gamma_{AB,ik}^{\text{fric}} \cdot (\mathbf{v}_i - \mathbf{v}_k) \end{aligned}$$

which can be abbreviated as

$$\mathbf{F}_i = \sum_j \Gamma_{ij} \cdot \mathbf{v}_j$$

for a system consisting of  $N$  nodes, where

$$\Gamma_{ij} = \begin{cases} \Gamma_{ii}^{\text{f}} + \sum_{k:k \neq i} \Gamma_{ik}^{\text{c}} + \sum_{(AB):i \in A} \sum_{k \in B} \Gamma_{AB,ik}^{\text{fric}}, & i = j, \\ -\Gamma_{ij}^{\text{c}} - \sum_{(AB):i \in A, j \in B} \Gamma_{AB,ij}^{\text{fric}}, & i \neq j. \end{cases}$$

The Cartesian components of the overall force vectors can be represented as a single  $(3N \times 1)$  column matrix, while the friction matrices can be assembled to a single  $(3N \times 3N)$  sparse symmetric positive definite friction matrix.<sup>14,54</sup> The conjugate gradient method is then used to efficiently solve the system for  $\{\mathbf{v}_j\}$  at each iteration. Positions of the nodes are subsequently updated using a forward Euler integration scheme.

We estimated  $\zeta = \frac{\eta^{\text{f}}}{2\gamma}$  as the characteristic timescale and used it to determine simulation time-step  $\delta t = \zeta/N$ . In order to minimize computational time without sacrificing accuracy, a small study was performed with varying  $N$ . Based on the convergence of output measures,  $N = 25$  was chosen.

A full simulation procedure took on average 60–80 h for a single setup, this was however heavily influenced by tissues size and tissue connectivity.

## Appendix B: tissue stress estimation

In order to estimate the macroscopic stress induced inside the tissue during compression, we need to find a suitable continuous representation of our discrete system. The typical approach how to describe a stress distribution in a continuous mechanics is to distribution of forces on a suitable elementary volume. On the tissue scale, a single cell is a natural choice for such an elementary volume.

We further assume that the Cauchy stress theorem is still valid for a macroscopic stress. Namely, we assume that the external force applied on a surface  $S$  of the cell  $\alpha$  can be fully characterized by cellular macroscopic stress  $\sigma_{\alpha}$ ,

$$\mathbf{F}_S^{\alpha} = \int_S d\mathbf{S}_{\alpha}(\mathbf{x}) \cdot \sigma_{\alpha}(\mathbf{x}).$$

In our model, external forces on the cell are mediated only by contact forces (6), contact frictions (17) and liquid drag (14). In the static (equilibrium) configuration the later two contributions



vanish. Consequently, we can formulate the Cauchy stress theorem for every contact pair  $(AB)$  as

$$\mathbf{F}_{AB}^{\text{adh}} = \int_{S_{AB}} d\mathbf{S}_\alpha(\mathbf{x}) \cdot \boldsymbol{\sigma}_\alpha(\mathbf{x}), \quad (19)$$

where the area of interest on the cell surface is the contact area  $S_{AB}$ . While for any area  $S$  not belonging to any contact pair, *i.e.*  $S \cap \bigcup_{(AB)} S_{AB} = \emptyset$ ,

$$\mathbf{0} = \int_S d\mathbf{S}_\alpha(\mathbf{x}) \cdot \boldsymbol{\sigma}_\alpha(\mathbf{x}). \quad (20)$$

The macroscopic stress  $\boldsymbol{\sigma}_\alpha$  on the cell  $\alpha$  is then a suitable candidate simultaneously fulfilling set of eqn (19) and (20). An obvious choice is the normal contact pressure

$$\sigma_\alpha^{\text{obv}} = - \sum_{(AB)} P_{AB}(\mathbf{x}) \hat{\mathbf{n}}_\alpha(\mathbf{x}) \otimes \hat{\mathbf{n}}_\alpha(\mathbf{x}).$$

However, such a choice is not suitable for characterizing the average mechanical conditions of cells at the tissue scale. On tissue scale the stress inside a cell can be considered uniform,  $\sigma_\alpha(\mathbf{x}) \equiv \sigma_\alpha$ . By imposing such strong assumption, we can no longer fulfill simultaneously all eqn (19) and (20). Moreover, due to the cell being in mechanical equilibrium without the presence of body forces, the mean square error defined by integrating all contributions over the cell surface  $S_\alpha$  is automatically zero,

$$\oint_{S_\alpha} d\mathbf{S}_\alpha(\mathbf{x}) \cdot \boldsymbol{\sigma}_\alpha = \sum_{(AB)} \mathbf{F}_{AB}^{\text{adh}} = \mathbf{0}.$$

A suitable candidate for an error function, inspired by the functional form of the virial stress, is

$$\begin{aligned} & \sum_{(AB)} \int_{S_\alpha} d\mathbf{S}_\alpha(\mathbf{x}) \cdot \boldsymbol{\sigma}_\alpha \cdot (\mathbf{x}_{AB} - \mathbf{x}_\alpha) \\ & + \sum_{S: S \cap \bigcup_{(AB)} S_{AB} = \emptyset} \int_{S_\alpha} d\mathbf{S}_\alpha(\mathbf{x}) \cdot \boldsymbol{\sigma}_\alpha \cdot (\mathbf{x}_A - \mathbf{x}_\alpha) \\ & = \sum_{(AB)} \mathbf{F}_{AB}^{\text{adh}} \cdot (\mathbf{x}_{AB} - \mathbf{x}_\alpha), \end{aligned}$$

which, in the limit of an infinitesimally fine triangulation, simplifies to

$$\oint_{S_\alpha} d\mathbf{S}_\alpha(\mathbf{x}) \cdot \boldsymbol{\sigma}_\alpha \cdot (\mathbf{x} - \mathbf{x}_\alpha) = \oint_{S_\alpha} d\mathbf{S}_\alpha(\mathbf{x}) \cdot (\mathbf{x} - \mathbf{x}_\alpha) \sum_{(AB)} P_{AB}^{\text{adh}}(\mathbf{x}).$$

Note, that unlike in the naive approach where contact pressures were weighted by the contact area, in this approach they are weighted by (triple) the volume of the conical section from the center of the cell to the contact area.

Assuming the macroscopic stress tensor is symmetric,  $\boldsymbol{\sigma}_\alpha = \boldsymbol{\sigma}_\alpha^T$ , and contact pressure on the cell surface  $P_{AB}^{\text{adh}}(\mathbf{x}) = \sum_{A \in \alpha} \sum_B P_{AB}^{\text{adh}}(\mathbf{x})$ ,

the equation can be further simplified to

$$\text{Tr} \boldsymbol{\sigma}_\alpha \cdot \oint_{S_\alpha} d\mathbf{S}_\alpha(\mathbf{x}) \otimes (\mathbf{x} - \mathbf{x}_\alpha) = \oint_{S_\alpha} d\mathbf{S}_\alpha(\mathbf{x}) \cdot (\mathbf{x} - \mathbf{x}_\alpha) P_\alpha^{\text{adh}}(\mathbf{x}),$$

where the integral can be further evaluated by using a generalized Stokes theorem

$$\oint_{S_\alpha} d\mathbf{S}_\alpha(\mathbf{x}) \otimes (\mathbf{x} - \mathbf{x}_\alpha) = V_\alpha \mathbb{I},$$

which leads to constraint

$$\text{Tr} \boldsymbol{\sigma}_\alpha = \frac{1}{V_\alpha} \oint_{S_\alpha} d\mathbf{S}_\alpha(\mathbf{x}) \cdot (\mathbf{x} - \mathbf{x}_\alpha) P_\alpha^{\text{adh}}(\mathbf{x}). \quad (21)$$

This quantity characterizes the macroscopic tension (pressure) inside a cell and is equivalent to the hydrostatic tension acting on the droplet replacement of the cell<sup>54</sup>

$$\sigma_\alpha^h = \frac{1}{3V_\alpha} \oint_{S_\alpha} d\mathbf{S}_\alpha(\mathbf{x}) \cdot (\mathbf{x} - \mathbf{x}_\alpha) P_\alpha^{\text{adh}}(\mathbf{x}).$$

## Appendix C: mechanical measures

To obtain the reported mechanical measures, we perform five independent repeats for each experimental condition. A statistical ensemble is generated by pooling the end states of these repeats. This ensemble is then used to determine the mean value and variances. To generate radial profiles, spatially distributed quantities were binned based on their relative position vector.

(1) For each node  $i$  of the triangulated representation of the cell, connected to  $N_i^\Delta$  triangles, the in-plane cortex tension eqn (2) is estimated as

$$\gamma_i^{\text{eff}} \approx \frac{1}{N_i^\Delta} \sum_{j:(ij)} \frac{\mathbf{F}_{ij}^{\text{el}} \cdot \hat{\mathbf{n}}_{ij}}{d_{ij} \tan \frac{\pi}{N_i^\Delta}},$$

where we weight in all spring tensions  $\mathbf{F}_{ij}^{\text{el}} \cdot \hat{\mathbf{n}}_{ij}/d_{ij}$ , *cf.* (8), from all connected nodes  $j$ .<sup>14</sup>

(2) The contact stress, eqn (3), is estimated for each triangle  $A$  by summing the contact forces  $\mathbf{F}_{AB}^{\text{adh}}$  for all contact pairs  $(AB)$ , *cf.* (6),

$$\sigma_{m,A}^c \approx \frac{1}{S_A} \sum_{B:(AB)} \mathbf{F}_{AB}^{\text{adh}} \cdot \hat{\mathbf{n}}_A,$$

where  $\hat{\mathbf{n}}_A$  and  $S_A$  are the normal unit vector and area of triangle  $A$ . The total contact force magnitude acting on the interface of cell pair  $(\alpha\beta)$  is then estimated as

$$\mathbf{F}_{\alpha\beta}^{\text{adh}} \approx \sum_{(AB): A \in \alpha \wedge B \in \beta} \mathbf{F}_{AB}^{\text{adh}} \cdot \hat{\mathbf{n}}_{\alpha\beta}$$

projecting all forces at the interface of cells  $\alpha$  and  $\beta$  to the direction  $\hat{\mathbf{n}}_{\alpha\beta} \propto \mathbf{x}_\alpha - \mathbf{x}_\beta$ .



(3) We estimate the hydrostatic stress expressed in eqn (4) (derivation provided in Appendix B) as

$$\sigma_{\alpha}^h \approx \frac{1}{3V_{\alpha}} \sum_{A \in \alpha} \sum_B F_{AB}^{\text{adh}} \cdot (\mathbf{x}_{AB} - \mathbf{x}_{\alpha}).$$

To increase the spatial resolution of cell related variables such as  $\sigma^h$  estimates, point probes were randomly distributed in the tissue aggregates. For a given setup, 10 000 probes were used to estimate the  $\sigma^h$  for a given location, interpolating between the values of the cellular nearest neighbors. This was done independently for the 5 replicas per setup. The results were binned based on the radial position inside of the tissue spheroid to generate the radial profiles reported in the main text.

## Appendix D: list of model parameters

**Table 2** Reference table of cell mechanical properties

Parameter	Symbol	Value	Unit
Cell radius	$R^{\text{cell}}$	5–13	$\mu\text{m}$
Effective cortical thickness	$t$	200	nm
Cortical stiffness	$E$	0.3125–320	kPa
Poisson's ratio cortex	$\nu$	1/3	—
Cortical tension	$\gamma$	0.5	$\text{nN } \mu\text{m}^{-1}$
Adhesive tension	$\omega$	0.0625–1	$\text{nN } \mu\text{m}^{-1}$
Cell count	$N$	75–600	—
Normal contact friction	$\gamma^{\parallel}$	0.05	$\text{kPa s } \mu\text{m}^{-1}$
Tangential contact friction	$\gamma^{\parallel}$	0.05	$\text{kPa s } \mu\text{m}^{-1}$
Cortical viscosity	$\eta$	1	$\text{kPa s}$
Fluid viscosity	$\eta^f$	0.05	$\text{kPa s}$
Bulk modulus cell	$K$	5	kPa
Integration time	$T_i$	0.115	s
Differentiation time	$T_d$	1.15	s
Time step	$\delta t$	3.85	ms

## Appendix E: simulated annealing

Simulated annealing-based approaches have been used to optimize 3D packing in general components layout problems. During the seeding phase, a simulated annealing procedure was used to generate compact granular piles. These piles were then used to initialize the aggregation simulations.

Our simulated annealing procedures are initialized by randomly seeding beads in the selected geometry with a density slightly lower than the close-packing density. Due to the distribution of cell radii and random placement, overlapping beads will be present. A linear repulsive force model was used to describe bead-bead contacts, minimizing bead overlaps. Random forces were introduced to agitate the beads, unjamming the system. The annealing procedure is achieved by an exponential decay of the mean magnitude of the random (Gaussian) force, while at the same time the stiffness of the repulsive potential is linearly increased. This means that the system effectively cools down to a (global) potential minimum, with a reduced chance of getting caught in local minima caused by bead jamming.

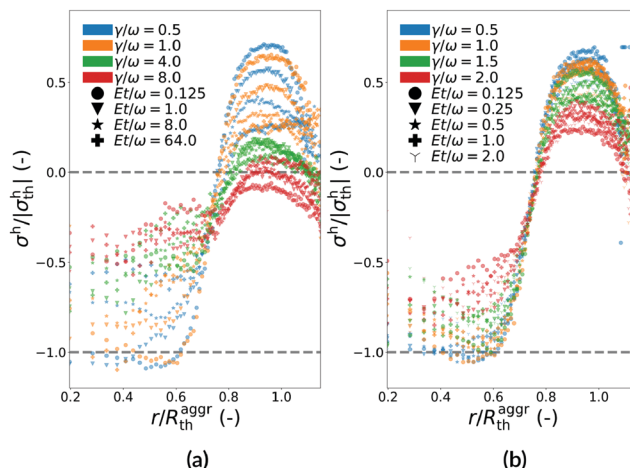


**Fig. 7** Comparison to liquid droplet mechanics. Normalized  $\sigma^h$  over normalized radial positions. For  $\omega$  dominated systems,  $\sigma^h$  approaches the tissue-scale Young–Laplace pressure  $\sigma_{\text{th}}^h$  in the core. (a) Broad parameter sweep. Overall  $\gamma/\omega$  seems to dominate the mechanical behavior for the cell. For low  $\gamma/\omega$ ,  $Et/\omega$  effects can be observed. However, as  $\gamma/\omega$  increases,  $Et/\omega$  effects become less pronounced. (b) Refined parameter sweep in the liquid limit. The trend ( $\sigma^h/\sigma_{\text{th}}^h$  scaling) evolves smoothly and is dominated by effects.

## Appendix F: the adhesive limit

In the soft adhesive limit, adhesive forces balanced by volume conservation forces dominate the system. In the bulk of the tissue, symmetry conditions (cell–cell contact in all directions) assure that the mean total adhesive force acting on a cell has no net direction. At the periphery, a net inward facing force (pointing towards the core of the aggregate) emerges as the adhesive forces over the cell surface are not symmetric at the tissue boundary. This is very analogous to how the surface tension of an isotropic material results from an imbalance of cohesive forces between the molecules. With this analogy, it can be seen that the cell–cell property (adhesive tension) emerges as a tissue-scale property (effective surface tension of the tissue) in this soft adhesive limit.

As  $\sigma^h$  represents the bulk tissue pressure, the relation between  $\sigma^h$  and adhesive tension  $\omega$  is then the result of the geometrical boundary conditions: mean tissue curvature  $2/R_{\text{th}}^{\text{aggr}}$ . This relation is described by the young–Laplace law  $\sigma_{\text{th}}^h = 2\omega/R_{\text{th}}^{\text{aggr}}$ .

However, and importantly, this only holds for very specific cases, where no external loads are applied on the tissue and when cell mechanical properties are within the adhesive limit, where the confluent tissue behaves as an isotropic material.

To investigate how  $\sigma^h$  converged to  $\sigma_{\text{th}}^h$ , a full parameter sweep was performed, see Fig. 7. As the trend scaled smoothly, a subset of the data was used in the main text as to not oversaturate the graph, see Fig. 4a and b.

## Appendix G: indentation simulations

To mechanically probe the spheroids generated in the aggregation phase, indentation simulations were performed. In our work we



opted to perform confined indentation experiments where a convex hull was fitted around the samples before being probed. The contact stiffness of these hulls should be sufficiently high to confine the samples during compression, while not being too high as to introduce numerical artifacts. As a probe we used a stiff bead with radius  $R^{\text{bead}} = 3R^{\text{cell}}$ . A Hertzian contact model with slip boundary conditions was used to model both cell-hull and cell probe interactions.

Using a force based controller, we indented the samples with a force of 15 nN, generating a force–displacement curve as the simulation progressed. Once the probe reached a stable position, cell–cell contact forces were extracted for further analysis, see main text.

## Acknowledgements

This work is part of Prometheus, the KU Leuven R&D Division for Skeletal Tissue Engineering. M. C. acknowledges support from the Research Foundation Flanders (FWO), grant 1S46817N. B. S. acknowledges support from the Research Foundation Flanders (FWO) grant 12Z6118N, and KU Leuven internal funding C14/18/055.

## Notes and references

- 1 F. Hirschhaeuser, H. Menne, C. Dittfeld, J. West, W. Mueller-Klieser and L. A. Kunz-Schughart, *J. Biotechnol.*, 2010, **148**, 3–15.
- 2 E.-M. Schoetz, M. Lanio, J. A. Talbot and M. L. Manning, *J. R. Soc., Interface*, 2013, **10**, 20130726.
- 3 K. Duval, H. Grover, L.-H. Han, Y. Mou, A. F. Pegoraro, J. Fredberg and Z. Chen, *Physiology*, 2017, **32**, 266–277.
- 4 K. Guevorkian, M.-J. Colbert, M. Durth, S. Dufour and F. Brochard-Wyart, *Phys. Rev. Lett.*, 2010, **104**, 218101.
- 5 D. Jaiswal, N. Cowley, Z. Bian, G. Zheng, K. P. Claffey and K. Hoshino, *PLoS One*, 2017, **12**, e0188346.
- 6 S. Ehrig, B. Schamberger, C. M. Bidan, A. West, C. Jacobi, K. Lam, P. Kollmannsberger, A. Petersen, P. Tomancak and K. Komareddy, *et al.*, *Sci. Adv.*, 2019, **5**, eaav9394.
- 7 S. Kim, M. Pochitaloff, G. Stooke-Vaughan and O. Campas, *Nat. Phys.*, 2021, 1–8, DOI: 10.1038/s41567-021-01215-1.
- 8 D. M. Mueth, H. M. Jaeger and S. R. Nagel, *Phys. Rev. E: Stat. Phys., Plasmas, Fluids, Relat. Interdiscip. Top.*, 1998, **57**, 3164.
- 9 B. Smeets, J. Pešek, T. Deckers, G. N. Hall, M. Cuvelier, S. Ongenaes, V. Bloemen, F. P. Luyten, I. Papantoniou and H. Ramon, *Matter*, 2020, 1283–1295.
- 10 O. Campàs, T. Mammoto, S. Hasso, R. A. Sperling, D. O'connell, A. G. Bischof, R. Maas, D. A. Weitz, L. Mahadevan and D. E. Ingber, *Nat. Methods*, 2014, **11**, 183.
- 11 M. Dolega, M. Delarue, F. Ingremeau, J. Prost, A. Delon and G. Cappelletto, *Nat. Commun.*, 2017, **8**, 14056.
- 12 A. A. Lucio, A. Mongera, E. Shelton, R. Chen, A. M. Doyle and O. Campàs, *Sci. Rep.*, 2017, **7**, 12022.
- 13 W. Lee, N. Kalashnikov, S. Mok, R. Halaoui, E. Kuzmin, A. J. Putnam, S. Takayama, M. Park, L. McCaffrey and R. Zhao, *et al.*, *Nat. Commun.*, 2019, **10**, 144.
- 14 T. Odenthal, B. Smeets, P. Van Liedekerke, E. Tijskens, H. Van Oosterwyck and H. Ramon, *PLoS Comput. Biol.*, 2013, **9**, e1003267.
- 15 B. Smeets, M. Cuvelier, J. Pešek and H. Ramon, *Biophys. J.*, 2019, **116**, 930–937.
- 16 S. Alt, P. Ganguly and G. Salbreux, *Philos. Trans. R. Soc., B*, 2017, **372**, 20150520.
- 17 P. Van Liedekerke, J. Neitsch, T. Johann, E. Warmt, I. G. Valverde, S. Grosser, S. Hoehme, J. Kaes and D. Drasdo, *bioRxiv*, 2019, DOI: 10.1101/470559.
- 18 Y.-S. Chu, S. Dufour, J. P. Thiery, E. Perez and F. Pincet, *Phys. Rev. Lett.*, 2005, **94**, 028102.
- 19 J.-L. Matre, H. Berthoumieux, S. F. G. Krens, G. Salbreux, F. Jülicher, E. Paluch and C.-P. Heisenberg, *Science*, 2012, **338**, 253–256.
- 20 H. Turler and J.-L. Maître, *Semin. Cell Dev. Biol.*, 2015, **47–48**, 110–117.
- 21 J. B. Lansman, T. J. Hallam and T. J. Rink, *Nature*, 1987, **325**, 811–813.
- 22 D. E. Leckband and J. De Rooij, *Annu. Rev. Cell Dev. Biol.*, 2014, **30**, 291–315.
- 23 J. Gao, L. He, Y. Shi, M. Cai, H. Xu, J. Jiang, L. Zhang and H. Wang, *Nanoscale*, 2017, **9**, 16993–17003.
- 24 D.-H. Kim, B. Li, F. Si, J. M. Phillip, D. Wirtz and S. X. Sun, *J. Cell Sci.*, 2015, **128**, 3375–3385.
- 25 J. Pannetier, J. Bassas-Alsina, J. Rodriguez-Carvajal and V. Caingnaert, *Nature*, 1990, **346**, 343.
- 26 L. Sui, S. Alt, M. Weigert, N. Dye, S. Eaton, F. Jug, E. W. Myers, F. Jülicher, G. Salbreux and C. Dahmann, *Nat. Commun.*, 2018, **9**, 1–13.
- 27 A. X. Cartagena-Rivera, J. S. Logue, C. M. Waterman and R. S. Chadwick, *Biophys. J.*, 2016, **110**, 2528–2539.
- 28 A. G. Clark, K. Dierkes and E. K. Paluch, *Biophys. J.*, 2013, **105**, 570–580.
- 29 M. Kot, H. Nagahashi and P. Szymczak, *Vis. Comput.*, 2015, **31**, 1339–1350.
- 30 J.-Y. Tinevez, U. Schulze, G. Salbreux, J. Roensch, J.-F. Joanny and E. Paluch, *Proc. Natl. Acad. Sci. U. S. A.*, 2009, **106**, 18581–18586.
- 31 M. Krieg, Y. Arboleda-Estudillo, P.-H. Puech, J. Käfer, F. Graner, D. Müller and C.-P. Heisenberg, *Nat. Cell Biol.*, 2008, **10**, 429.
- 32 E. Mohagheghian, J. Luo, J. Chen, G. Chaudhary, J. Chen, J. Sun, R. H. Ewoldt and N. Wang, *Nat. Commun.*, 2018, **9**, 1–14.
- 33 K. Guevorkian, M.-J. Colbert, M. Durth, S. Dufour and F. Brochard-Wyart, *Phys. Rev. Lett.*, 2010, **104**, 218101.
- 34 R. Winklbauer, *J. Cell Sci.*, 2015, **128**, 3687–3693.
- 35 R. Shuttleworth, *Proc. Phys. Soc., London, Sect. A*, 1950, **63**, 444.
- 36 M. A. Wozniak and C. S. Chen, *Nat. Rev. Mol. Cell Biol.*, 2009, **10**, 34–43.
- 37 J. J. Northey, L. Przybyla and V. M. Weaver, *Cancer Discovery*, 2017, **7**, 1224–1237.





- 38 G. Cheng, J. Tse, R. K. Jain and L. L. Munn, *PLoS One*, 2009, **4**, e4632.
- 39 I. C. Berg, E. Mohagheghian, K. Habing, N. Wang and G. H. Underhill, *bioRxiv*, 2021, DOI: 10.1101/2020.10.28.355875.
- 40 C.-P. Heisenberg and Y. Bellache, *Cell*, 2013, **153**, 948–962.
- 41 T. Lecuit, P.-F. Lenne and E. Munro, *Annu. Rev. Cell Dev. Biol.*, 2011, **27**, 157–184.
- 42 M. Sadati, N. T. Qazvini, R. Krishnan, C. Y. Park and J. J. Fredberg, *Differentiation*, 2013, **86**, 121–125.
- 43 R. Changede and M. Sheetz, *BioEssays*, 2017, **39**, 1–12.
- 44 P.-F. Lenne, J.-F. Rupprecht and V. Viasnoff, *Dev. Cell*, 2021, **56**, 202–212.
- 45 R. Winklbauer, *J. Cell Sci.*, 2019, **132**, jcs231597.
- 46 J. N. Israelachvili, *Intermolecular and surface forces*, Academic Press, 2011.
- 47 B. Smeets, T. Odenthal, S. Vanmaercke and H. Ramon, *Comput. Methods Appl. Mech. Eng.*, 2015, **290**, 277–289.
- 48 L. Zhang, T. Cui and H. Liu, *J. Comput. Math.*, 2009, **27**, 89–96.
- 49 A. V. Gelder, *J. Graph. Tools*, 1998, **3**, 21–41.
- 50 D. Fedosov, B. Caswell and G. Karniadakis, *Comput. Methods Appl. Mech. Eng.*, 2010, **199**, 1937–1948.
- 51 D. Fedosov, PhD thesis, Brown University, 2010.
- 52 P. Van Liedekerke, B. Smeets, T. Odenthal, E. Tijskens and H. Ramon, *Comput. Phys. Commun.*, 2013, **184**, 1686–1696.
- 53 E. M. Purcell, *Am. J. Phys.*, 1977, **45**, 3–11.
- 54 P. Van Liedekerke, M. M. Palm, N. Jagiella and D. Drasdo, *Comput. Part. Mech.*, 2015, **2**, 401–444.

